The cooling, mass and radius of the neutron star in EXO 0748-676 in quiescence with XMM-Newton

Cheng, Zheng; Mendez, Raúl; Díaz-Trigo, María; Costantini, Elisa

Published in:
Monthly Notices of the Royal Astronomical Society

DOI:
10.1093/mnras/stx1452

Monthly Notices
of the
ROYAL ASTRONOMICAL SOCIETY

MNRAS **471,** 2605–2615 (2017)
Advance Access publication 2017 June 12

doi:10.1093/mnras/stx1452

The cooling, mass and radius of the neutron star in EXO 0748−676 in quiescence with *XMM–Newton*

Zheng Cheng,[1]★ Mariano Méndez,[1] María Díaz-Trigo[2] and Elisa Costantini[3]

[1] *Kapteyn Astronomical Institute, University of Groningen, Postbus 800, NL-9700 AV Groningen, the Netherlands*
[2] *ESO, Karl-Schwarzschild-Strasse 2, D-85748 Garching bei München, Germany*
[3] *SRON, Netherlands Institute for Space Research, Sorbonnelaan 2, NL-3584 CA Utrecht, the Netherlands*

Accepted 2017 June 8. Received 2017 June 7; in original form 2017 February 3

ABSTRACT

We analyse four *XMM–Newton* observations of the neutron-star low-mass X-ray binary EXO 0748−676 in quiescence. We fit the spectra with an absorbed neutron-star atmosphere model, without the need for a high-energy (power-law) component; with a 95 per cent confidence the power law contributes less than 1 per cent to the total flux of the source in 0.5–10.0 keV. The fits show significant residuals at around 0.5 keV which can be explained by either a hot gas component around the neutron star or a moderately broad emission line from a residual accretion disc. The temperature of the neutron star has decreased significantly compared to the previous observation, from 124 to 105 eV, with the cooling curve being consistent with either an exponential decay plus a constant or a (broken) power law. The best-fitting neutron-star mass and radius can be better constrained if we extend the fits down to the lowest possible energy available. For an assumed distance of 7.1 kpc, the best-fitting neutron-star mass and radius are $2.00^{+0.07}_{-0.24}$ $M_{\odot}$ and $11.3^{+1.3}_{-1.0}$ km if we fit the spectrum over the 0.3–10 keV range, but $1.50^{+0.4}_{-1.0}$ $M_{\odot}$ and $12.2^{+0.8}_{-3.6}$ km if we restrict the fits to the 0.5–10 keV range. We finally discuss the effect of the assumed distance to the source upon the best-fitting neutron-star mass and radius. As systematic uncertainties in the deduced mass and radius depending on the distance are much larger than the statistical errors, it would be disingenuous to take these results at face value.

Key words: dense matter – equation of state – stars: individual: EXO 0748−676 – stars: neutron – X-rays: binaries.

1 INTRODUCTION

EXO 0748−676 is an X-ray transient that was discovered using the *European X-ray Observatory* (*EXOSAT*) in 1985 (Parmar et al. 1986). The source exhibits 8.3-min duration X-ray eclipses that recur with a period of 3.82 h. The periodic X-ray eclipses and irregular X-ray dips indicate that the system is a low-mass X-ray binary (LMXB) at a relative high inclination angle. Parmar et al. (1986) estimated that the inclination of the system lies in the range 75°–82°. Gottwald et al. (1986) detected type I X-ray bursts in this source, and therefore identified the compact object as a neutron star (NS). Homan & van der Klis (2000) reported a 695-Hz quasi-periodic oscillation (QPO) in an observation with the *Rossi X-ray Timing Explorer* (*RXTE*). Villarreal & Strohmayer (2004) detected a 45-Hz oscillation in the average power spectrum of 38 X-ray bursts, which they interpreted as the spin frequency of the NS. Galloway et al. (2010) detected a 552-Hz oscillation in the rising phase of two type I X-ray bursts, and concluded that this is the spin frequency of EXO 0748−676, rather than the 45-Hz oscillation.

Wolff et al. (2005) detected a few unusually strong X-ray bursts with a peak flux that was approximately four times higher than that of the normal bursts. They interpreted this as photospheric radius expansion (PRE) bursts, which indicated that the Eddington luminosity was reached at the peak of those bursts. Assuming a typical NS mass of 1.4 $M_{\odot}$, Wolff et al. (2005) derived a distance to EXO 0748−676 of 7.7 kpc for a helium-dominated photosphere, and 5.9 kpc for a hydrogen-dominated photosphere. By considering the touchdown flux and the high orbital inclination of the system, Galloway et al. (2008b) estimated a distance of 7.1 ± 1.2 kpc (see also Galloway, Özel & Psaltis 2008a).

In 2008, observations with the Proportional Counter Array on-board *RXTE* (Wolff, Ray & Wood 2008a) and the *Swift X-Ray Telescope* (Wolff et al. 2008b) showed that the X-ray flux of EXO 0748−676 was declining, indicating that accretion was ceasing and the source was transitioning to quiescence after accreting for over 24 yr. This transition made it possible to study the cooling process of this source (Degenaar et al. 2011, 2014; Díaz Trigo et al. 2011; Zhang et al. 2011).

★ E-mail: zheng@astro.rug.nl

Isolated NS mainly cool via neutrino emission from the stellar core and photon emissions from the surface (Yakovlev & Pethick 2004). For a quasi-persistent X-ray binary like EXO 0748−676, the outburst phase can last from years to decades, and pycnonuclear reactions can cause a significant temperature gradient between the core and the crust (Degenaar et al. 2011). When accretion ends, the crust is expected to thermally relax on a time-scale of years, which can provide us with information on the properties of the NS crust (Haensel & Zdunik 2008; Brown & Cumming 2009).

In this paper we present the spectral analysis of four *XMM–Newton* observations of EXO 0748−676 in quiescence. The first three of these observations were already analysed by Díaz Trigo et al. (2011), while the last observation was obtained about 3 yr after the previous one, providing a long baseline to study the cooling process of EXO 0748−676. We describe the details of the observations and the data reduction and analysis in Section 2, show the results in Section 3 and discuss our findings in Section 4.

2 DATA REDUCTION AND ANALYSIS

EXO 0748−676 was observed with *XMM–Newton* on 2008 November 6 at 08:30−16:42 UTC, just after it turned into quiescence (obsID 0560180701, see also Zhang et al. 2011), and subsequently four more times from 2009 March 18 to 2013 April 15. Zhang et al. (2011) found that, besides the thermal emission from the NS, in the first observation there is a significant contribution of a non-thermal component. Díaz Trigo et al. (2011) found that the non-thermal component was not present in the following three observations. Here we find (see below) that the same is true in the last observation and, therefore, in the rest of the paper we only analyse the last four *XMM–Newton* observations of this source.

Data were collected simultaneously with the European Photon Imaging Cameras (EPIC; Strüder et al. 2001) and the Reflection Grating Spectrometers (RGS; den Herder et al. 2001). The EPIC cameras consist of one PN and two metal oxide semiconductor (MOS) detectors, which offer sensitive imaging observations over a field of view of 30 arcmin and an energy range from 0.15 to 12 keV, while the two RGS instruments cover the range between 0.3 and 2.0 keV with a resolution of 100–500. We give the log of the observations in Table 1.

We reduced the *XMM–Newton* Observation Data Files using the SCIENCE ANALYSIS SOFTWARE (SAS) version 14.0.0. We extracted the event files for the PN and the two MOS detectors using the tasks *epproc* and *emproc*, respectively, and we processed the RGS data using the task *rgsproc*; following the recommendations of the *XMM–Newton* team, in all cases we used the default parameters of these tasks. Since the source was very weak during all these observations, the RGS instruments collected very few photons (both RGS combined contained less than 5 per cent of the photons of the PN and MOS instruments combined) and, therefore, in the rest of the paper we only fit the PN and MOS data. We, however, checked that the best-fitting parameters do not change significantly if we also include the RGS data to the fits. We mention this when necessary.

In order to identify the existence of possible flaring particle background, we extracted light curves for energies larger than 10 keV for MOS and in the 10–12 keV range for PN. We found soft proton flares in the MOS data of observation 0651690101 and in small parts of the PN data of all observations. Following Piconcelli et al. (2004), we calculated the cumulative signal-to-noise ratio (SNR), as a function of the background count rate for all cameras in all observations. We found that in all cases the cumulative SNR increases monotonically up to the highest background count rates, indicating that, for these observations, it is better not to filter out the particle background flares. Nevertheless, to assess the effect of the background flares upon our analysis, we defined good intervals, GTI, as the times in which the count rate in the above bands was below 0.35 count s^{-1} for MOS and 0.40 count s^{-1} for PN. We applied these GTI files, together with standard filters, to the event data, and we subsequently removed the exposure time range during the eclipses (see Section 1). We also extracted spectra without removing the flaring time (but excluding the eclipses), and found that these spectra were consistent with those for which we had excluded the flares. Therefore, in the rest of the paper we do not filter out the flaring time in the data.

Table 1. *XMM–Newton* observational data log of EXO 0748−676.

Observation ID	Date	Instrument	Exposure time (ks)
0605560401	2009-03-18	PN	36.27
		MOS1	43.15
		MOS2	42.04
		RGS1	47.00
		RGS2	45.44
0605560501	2009-07-01	PN	86.16
		MOS1	99.60
		MOS2	99.60
		RGS1	101.20
		RGS2	101.30
0651690101	2010-06-17	PN	24.80
		MOS1	29.62
		MOS2	29.98
		RGS1	30.22
		RGS2	30.36
		PN	58.88
		MOS1	67.44
		MOS2	67.48
		RGS1	70.78
		RGS2	70.74
0690330101	2013-04-15	PN	91.32
		MOS1	103.00
		MOS2	103.10
		RGS1	104.20
		RGS2	104.30

We extracted source spectra in the 0.3–10.0 keV band from a circular region with a radius of 35 arcsec centred on the source, and the corresponding background spectra from a source-free region with a radius of 35 arcsec, using the SAS task *evselect*. We confirmed that the data were not piled up using the task *epatplot*. We created the photon redistribution matrices (RMF) and ancillary response file (ARF), and re-binned the spectra to have at least 25 counts per channel using the task *grppha*.

We fitted the spectra in the 0.3–10.0 keV band using XSPEC version of 12.8.2. We fitted all four observations, in total 15 spectra, simultaneously (see Table 1). We modelled the spectra using the NS hydrogen atmosphere model NSATMOS (Heinke et al. 2006). This model covers a wide range of surface gravity and effective temperature, including thermal electron conduction and self-irradiation by photons from the compact object, assuming an NS with a pure hydrogen atmosphere and a magnetic field of less than 10^9 G. The fitting parameters of NSATMOS include the unredshifted effective temperature of the NS ($T_{\rm eff}$), the NS gravitational mass ($M_{\rm ns}$), the NS radius ($R_{\rm ns}$), the distance to the source (D), and the fraction of the NS surface that is emitting (K), which we fixed to 1 throughout this work. We initially fixed the distance to 7.1 kpc and kept the NS

mass and radius free. In order to compare the temperature evolution during the quiescent state of EXO 0748−676 with the results of Degenaar et al. (2011), we subsequently fixed the NS mass, radius and distance to 1.4 $M_\odot$, 15.6 km and 7.4 kpc, respectively. The temperature for different instruments was linked to be the same value in the same observation, but was allowed to change freely among different observations.[1] To fit the positive residuals at around 0.5 keV, we included a collisionally ionized diffuse gas model VAPEC (Smith et al. 2001) in the fit. The parameters of this model are the plasma temperature, linked to be the same value for different instruments in the same observation, but allowed to change freely among different observations, the abundance of corresponding elements relative to the solar abundance, the redshift to the source (fixed to 0 in this analysis) and a normalization. We considered the effect of interstellar absorption by including the component PHABS in XSPEC using the abundance tables of Wilms, Allen & McCray (2000) with the photoelectric absorption cross-sections from Balucinska-Church & McCammon (1992) and the He cross-section by Yan, Sadeghpour & Dalgarno (1998). We also tested our fit using the abundance tables from Anders & Grevesse (1989) and the cross-sections from Verner et al. (1996), respectively. It turned out that the selection of cross-sections did not change the result at all, while the choice of interstellar abundance does have an influence on the result, we mention this when necessary. We linked the hydrogen column density along the line of sight, $N_{\rm H}$, across all observations but left it free to change. We included a multiplicative factor to account for the different efficiency between different instruments. This factor was fixed to 1 for all PN data, and was left free but kept the same for all the MOS1 and MOS2 data separately.

3 RESULTS

3.1 Spectra

In previous analyses of the quiescent emission of EXO 0748−676, the spectrum was usually fitted with a thermal component plus a power law with a photon index of ∼1.0–1.7 (Degenaar et al. 2011, 2014; Díaz Trigo et al. 2011; Zhang et al. 2011). We therefore initially tried the same model, CONST*PHABS*(NSATMOS + POWERLAW) in XSPEC with all parameters free. However, the parameters could not be well constrained unless we fixed the distance to the source. Here we adopted the value $D = 7.1$ kpc given by Galloway et al. (2008a). We also fixed the power-law index to 1.7, the same value used by Degenaar et al. (2011), which yields a χ^2 of 3739 for 3674 degrees of freedom. The power-law component is, however, not significantly required to fit the data in any of the observations; the 95 per cent confidence upper-limit of the power-law normalization for the four observations is in the range 1.0–6.0 × 10^{-6} photons cm^{-2} s^{-1} keV^{-1} at 1 keV, which translates into an upper limit of the power-law flux of less than 1 per cent of the total unabsorbed flux. This result does not change if we let the power-law index to vary between different observations; therefore we do not include a power law to the model. The best fit with the model CONST*PHABS*NSATMOS yields a χ^2 of 3774 for 3681 degrees of freedom, and the best-fitting parameters are $N_{\rm H} = (5.52^{+0.25}_{-0.30}) \times 10^{20}$ cm^{-2}, $M_{\rm ns} = 2.00^{+0.07}_{-0.23}$ $M_\odot$ and $R_{\rm ns} = 11.3 \pm 1.2$ km, respectively. (Unless otherwise stated, all errors correspond to the 90 per cent confidence interval for a single interesting parameter.) The hydrogen column density is slightly lower than the range, $N_{\rm H} = (0.7 - 1.2) \times 10^{21}$ cm^{-2}, found during outburst by Sidoli, Parmar & Oosterbroek (2005), but it is consistent with the value found by Degenaar et al. (2011), Díaz Trigo et al. (2011) and Zhang et al. (2011) in quiescence. The best-fitting temperatures for the four observations are 165 ± 16, 161 ± 15, 160 ± 15 and 154 ± 15 eV, respectively.[2] If we remove the flaring period in the spectra, the fit yields a χ^2 of 3120 for 3065 degrees of freedom, and the best-fitting hydrogen column density, NS mass and radius are $N_{\rm H} = (5.53^{+0.34}_{-0.30}) \times 10^{20}$ cm^{-2}, $M_{\rm ns} = 1.99^{+0.09}_{-0.26}$ $M_\odot$ and $R_{\rm ns} = 11.4 \pm 1.4$ km, respectively. The best-fitting temperatures for the four observations are 165 ± 16 eV, 161 ± 15 eV, 160 ± 15 eV and 153 ± 15 eV, respectively. All parameters are consistent, but with slightly larger error bars, compared with those obtained when we do not exclude the flares. The best-fitting parameters do not change significantly if we also add the RGS spectra (in the range 0.3–1.8 keV) to the fits.

All the fits, however, show positive residuals at around 0.5 keV (see bottom panel of Fig. 1). We therefore added a hot gas component, VAPEC, in the analysis. The temperature and normalization of this collisionally ionized plasma are linked to be the same for different instruments in the same observation but allowed to change freely among different observations. We initially set the gas

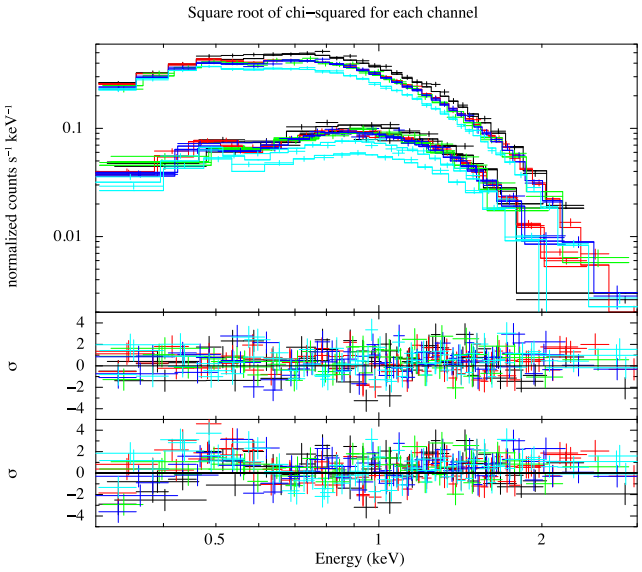

Figure 1. The 15 *XMM–Newton* EPIC spectra of EXO 0748−676 with the best-fitting model. Top panel: fits with the model CONST * PHABS * (NSATMOS + VAPEC) in the 0.3–10 keV range. The best-fitting NS mass and radius are $M_{\rm ns} = 2.05^{+0.09}_{-0.39}$ $M_\odot$ and $R_{\rm ns} = 11.4 \pm 2.1$ km, respectively. The best-fitting nitrogen abundance $Z_{\rm N} = 21 \pm 8$; the temperature of the hot gas for the four observations are 269 ± 43, 172 ± 13, 250 ± 29 and 152 ± 16 eV, respectively. (All errors represent the 90 per cent confidence interval of the given parameter for a single interesting parameter.) For plotting purposes we have re-binned the data by a factor of 8. Middle panel: the residuals, (data−model)/error, with respect to the best-fitting model. Bottom panel: the fitting residuals of the best-fitting model after removing the VAPEC component. We plot the PN, MOS1 and MOS2 spectra and models of each observation listed in Table 1 in black, red, green, blue and light blue, respectively.

[1] There are two separate, but consecutive, observations on 2010 June 17 under the same observation ID (see Table 1). Here we linked the effective temperature to be the same in both.

[2] These are the temperatures of the NS atmosphere, not the temperatures seen by an observer at infinity.

abundance of C, N and O free at first. The fitting result yields an oxygen abundance $Z_{\rm O} = 1.1^{+2.8}_{-0.5}$, consistent with solar abundance within errors. The fit is insensitive to the carbon abundance; the best-fitting result gives $\chi^2 = 3620.2$ with $Z_{\rm C} = 0.007$ compared to $\chi^2 = 3620.6$ when $Z_{\rm C}$ =1. Hence, we fixed the carbon and oxygen abundance to solar abundance in the rest of the analysis. Since the normalizations of the VAPEC component are consistent within errors for different observations, we linked them to be the same in all observations. The best fit with the model CONST*PHABS*(NSATMOS+VAPEC) gives a χ^2 of 3620 for 3675 degrees of freedom. In this case, $N_{\rm H}$ is $(7.8 \pm 0.5) \times 10^{20}\,{\rm cm}^{-2}$, and the temperature for the four observations is 167 ± 28, 162 ± 28, 160 ± 26 and 155 ± 27 eV, respectively (see footnote 2). The best-fitting NS mass and radius are $M_{\rm ns} = 2.05^{+0.09}_{-0.39}\,{\rm M}_{\odot}$ and $R_{\rm ns} = 11.4 \pm 2.1$ km, respectively. Again, the best-fitting parameters do not change significantly if we also add the RGS spectra to the fits. The best-fitting nitrogen abundance is 21 ± 8 solar abundance, and the temperature of the hot gas for the four observations is 269 ± 43, 172 ± 13, 250 ± 29 and 152 ± 16 eV, respectively. The *F*-test probability for a chance improvement when adding this collisionally ionized gas component to the model is 2×10^{-30}, which indicates that the addition of this component significantly improves the fit. Since the applicability of the *F*-test in these cases is questionable (Protassov et al. 2002), to check this we simulated 10^4 spectra of the model without this hot gas component and fitted these spectra with the model that includes VAPEC. None of these simulated spectra showed a normalization as strong (or stronger) than the one we found from the fits to the data, which shows that the probability that this hot gas component is due to a statistical fluctuation that is less than 10^{-4}. We did not find any significant edge in the effective area of the detectors around this energy that could, due to calibration uncertainties, account for these residuals.

We explored whether the residuals at around 0.5 keV could be due to the cross-section and abundance tables used in the model that fits the interstellar absorption. To test this, we fitted the spectra with the model without the hot gas component using the cross-section table of Verner et al. (1996) and the abundances of Anders & Grevesse (1989), but the residuals did not disappear, and the hot gas component was still significantly required by the fits. We also tried replacing the component PHABS by either VPHABS or TBNEW (the newest version of TBABS; Wilms et al. 2000), which allows us to change the abundance of the individual elements separately. One at a time, we let the abundance of N, O, Ne and Fe free, but the residuals remained, and in all cases the best-fitting abundances became either very low or very high. Finally, we added an extra edge to the model to check whether the line could be a calibration artefact related to the oxygen edge in the detectors. We fixed the energy of this edge in the model to 0.538 keV, the energy of the OI edge, and we allowed the normalization of the edge to be either positive or negative to account for, respectively, a lower or higher amount of oxygen contamination in the detectors relative to the values in the *XMM–Newton* calibration files. Since the positive residuals in our fits appear at somewhat lower energy than that of the OI edge, this procedure did not improve the fit. In summary, none of these alternatives could explain the residuals, and we therefore continued including this additional component in our model.

In Fig. 1 we show the spectra and the best-fitting model with (middle panel) and without (bottom panel) the hot gas component,

[2] These are the temperatures of the NS atmosphere, not the temperatures seen by an observer at infinity.

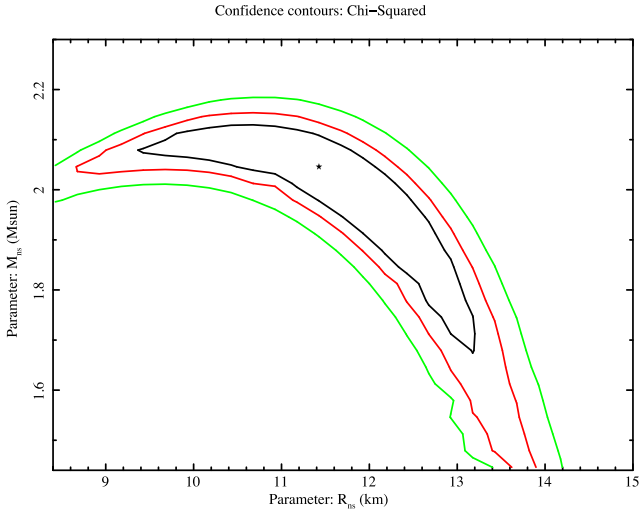

Figure 2. Contour plot of the mass and radius parameters of the NS in EXO 0748−676. We fitted the model CONST*PHABS*(NSATMOS+VAPEC) in the energy range 0.3–10.0 keV with the distance to the source fixed to 7.1 kpc. The cross marks the best-fitting mass and radius, $M_{\rm ns} = 2.05\,{\rm M}_{\odot}$ and $R_{\rm ns}$ = 11.4 km, respectively. The three contour lines represent the confidence levels of 68 per cent (black), 90 per cent (red) and 99 per cent (green) for two parameters.

and in Fig. 2 we show the contour plot of the mass and radius obtained from the fits.

In order to compare the temperature of the NS in EXO 0748−676 in our *XMM–Newton* observations with the temperature in the *Chandra* and *Swift* observations in Degenaar et al. (2011), we fixed the mass and the radius of the NS and the distance to the source to the same values used by Degenaar et al. (2011), $M_{\rm ns} = 1.4\,{\rm M}_{\odot}$, $R_{\rm ns} = 15.6$ km and $D = 7.4$ kpc. In this case the best-fitting model gives $N_{\rm H} = (9.1 \pm 0.5) \times 10^{20}\,{\rm cm}^{-2}$ and the nitrogen abundance of the hot gas component is $Z_{\rm N} = 24^{+11}_{-6}$, with a χ^2 of 3657 for 3677 degrees of freedom. We then calculated the effective temperature of the NS seen by an observer at infinity, $kT^{\infty}_{\rm eff}$, using the formula $kT^{\infty}_{\rm eff} = kT_{\rm eff}(1 - R_{\rm s}/R_{\rm NS})^{1/2}$, where $kT_{\rm eff}$ is the best-fitting temperature in our models, $R_{\rm s} = 2GM_{\rm NS}/c^2$, G is the gravitational constant and c is the speed of light. The NS effective temperatures at infinity for the four observations are given in Table 2. We also fitted the spectra without the hot gas component to check whether this component had an effect on the best-fitting temperatures; in this case the best fit gives $N_{\rm H} = (6.7 \pm 0.2) \times 10^{20}\,{\rm cm}^{-2}$ with a χ^2 of 3852 for 3683 degrees of freedom, and the NS effective temperatures at infinity for the four observations are given in Table 2.

The average flux from the hot gas component is about $5.8 \times 10^{-14}\,{\rm erg\,cm}^{-2}\,{\rm s}^{-1}$, which is about 7–10 per cent of the total flux in the energy range from 0.3 to 10.0 keV. The inclusion of this component in the model does not change the temperatures of the NS significantly as shown in Table 2.

3.2 Cooling curves

In our analysis we assumed the same NS mass, radius and source distance as Degenaar et al. (2011), which allows us to compare the effective temperature in our work with those in their work. Therefore, we combined our temperatures with those obtained by Degenaar et al. (2011) from *Chandra*, *Swift* and previous *XMM–Newton* observations.

Table 2. Fitting results to the spectra of EXO 0748−676.

Observation ID	MJD	NS $kT_{\rm eff}^{\infty}$ (eV) without VAPEC	NS $kT_{\rm eff}^{\infty}$ (eV) with VAPEC	$kT_{\rm gas}$ (eV)	$F_{\rm X}$ (10^{-12} erg cm^{-2}s^{-1})	$F_{\rm bol}^{\rm th}$ (10^{-13} erg cm^{-2} s^{-1})	VAPEC fraction (per cent)
0605560401	54908	112.1 ± 0.3	112.7 ± 0.3	241 ± 34	9.45 ± 0.19	9.97 ± 0.21	7.4 ± 1.8
0605560501	55013	108.8 ± 0.2	109.5 ± 0.3	164 ± 13	8.45 ± 0.17	8.78 ± 0.16	9.8 ± 1.5
0651690101	55364	108.1 ± 0.2	108.6 ± 0.2	231 ± 28	8.12 ± 0.16	8.49 ± 0.16	6.9 ± 1.5
0690330101	56397	104.3 ± 0.2	104.9 ± 0.3	141 ± 13	7.05 ± 0.15	7.31 ± 0.15	10.0 ± 1.7
χ^2 /d.o.f.		3852/3683	3657/3677				

Note. Best-fitting results for the model CONST*PHABS*(NSATMOS+VAPEC) fixing the NS mass, radius and distance to 1.4 $M_{\odot}$, 15.6 km and 7.4 kpc, respectively. The best-fitting equivalent hydrogen column density $N_{\rm H} = (9.1 \pm 0.5) \times 10^{20}$ cm^{-2}, and the nitrogen abundance of the hot gas component, is 24^{+11}_{-6} times solar abundance. The two columns under NS $kT_{\rm eff}^{\infty}$ show the NS effective temperature at infinity for the model with and without the hot gas component, respectively. The column $kT_{\rm gas}$ shows the corresponding temperature of the hot gas component in each observation. $F_{\rm X}$ is the unabsorbed model flux in the 0.3–10.0 keV band, and $F_{\rm bol}^{th}$ is the 0.01–100.0 keV unabsorbed flux of the NSATMOS component. VAPEC fraction is the fractional contribution of the hot gas component to the total unabsorbed flux in the 0.3–10.0 keV energy range.

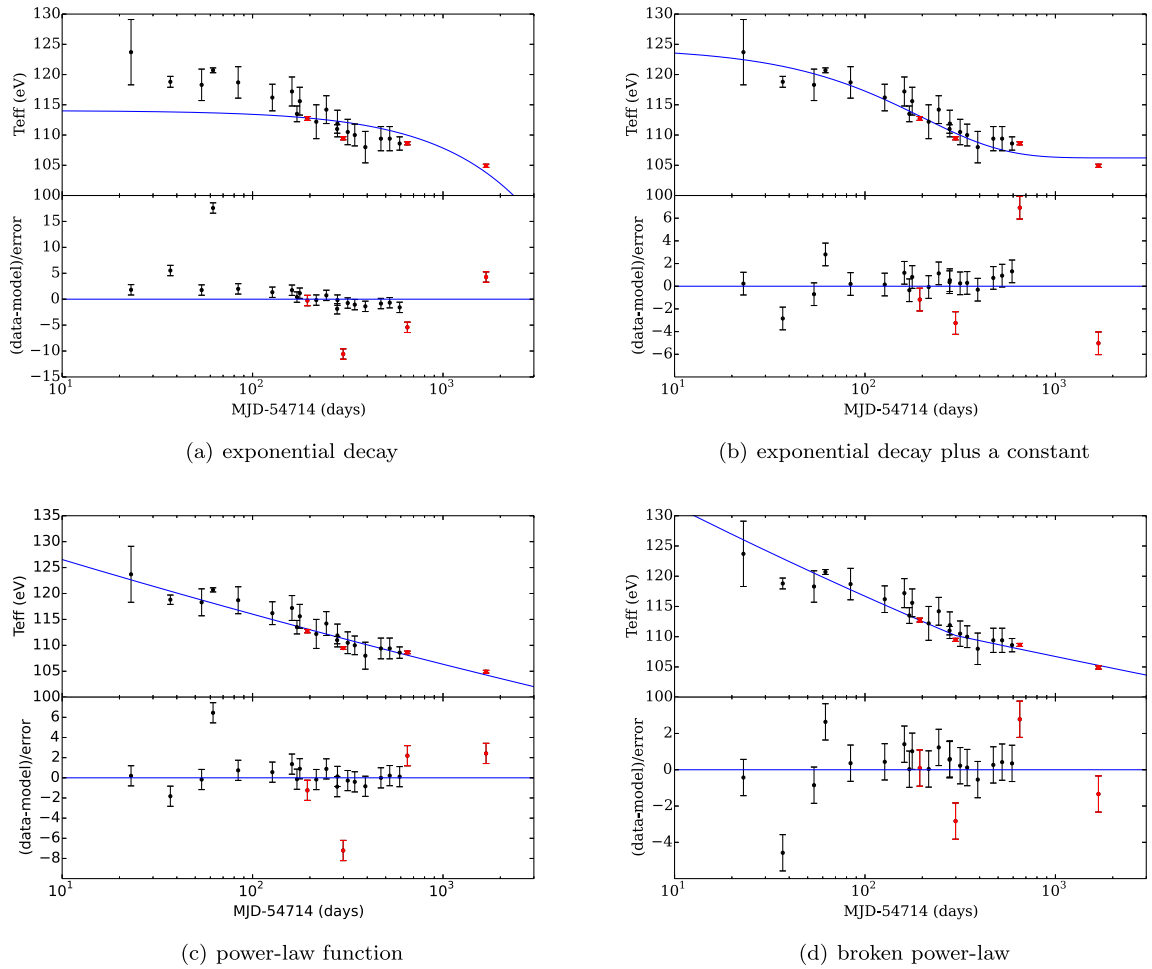

(a) exponential decay

(b) exponential decay plus a constant

(c) power-law function

(d) broken power-law

Figure 3. Effective temperature evolution of EXO 0748−676 fitted with different functions: exponential decay (upper left panel), exponential decay plus a constant offset (upper right panel), power-law decay (lower left panel) and broken power-law decay (lower right panel). The red circles represent the data obtained from the *XMM–Newton* observations in this paper; the black circles show the *Chandra*, *Swift* data and the first *XMM–Newton* observation presented here that were used in the analysis of Degenaar et al. (2011). The start date MJD 54714, corresponding to 2008 September 5, is the same date chosen by Degenaar et al. (2011).

In order to investigate the temperature evolution, we first fit the effective temperature versus time with an exponential function, $T_{\rm eff} = a{\rm e}^{-(t-t_0)/b}$; the fit yields $a = 114.1 \pm 0.9$ eV with an e-folding time of $17\,844 \pm 3124$ d. (The start time of the cooling was fixed at $t_0 = 54714$ MJD days as in Degenaar et al. 2011.) The result of this fit is shown in the upper left panel of Fig. 3. The fit is not good, with reduced χ^2 and χ^2_{ν} of 25 for 21 degrees of freedom. We then introduced an additional constant offset c in the exponential function. This model gives a better fit ($\chi^2_{\nu} = 6$ for 20 degrees of freedom) with $a = 18.2 \pm 1.4$ eV, $b = 200 \pm 27$ d, and the constant offset $c = 106.2 \pm 0.5$ eV. The result is shown in the upper right panel of Fig. 3. We also fitted a power law and a broken

Table 3. Fitting results of the cooling curve of EXO 0748−676.

Exponential decay $y(t) = ae^{-(t-t_0)/b}$	
Normalization factor, a	114.1 ± 0.9 eV
e-folding time, b	17844 ± 3124 d
χ^2 (d.o.f.)	528 (21)
Exponential decay with constant offset $y(t) = ae^{-(t-t_0)/b} + c$	
Normalization factor, a	18.2 ± 1.4 eV
e-folding time, b	200 ± 27 d
Constant offset, c	106.2 ± 0.5 eV
χ^2 (d.o.f.)	109 (20)
Power law $y(t) = a(t - t_0)^{-b}$	
Normalization factor, a	138.0 ± 2.1 eV
Power-law index, b	0.04 ± 0.01
χ^2 (d.o.f.)	115 (21)
Broken power law $y(t) = a(t - t_0)^{-b}, t - t_0 \leq t_b$; $a(t - t_0 - t_b)(t - t_0)^c, t - t_0 > t_b$	
Normalization factor, a	148.5 ± 3.5 eV
Power-law index b	0.05 ± 0.01
Power-law index c	0.03 ± 0.01
Break point t_0	299 ± 73 d
χ^2 (d.o.f.)	53 (19)

Note. All errors correspond to the 1σ confidence levels.

power law to the data, as proposed by Brown & Cumming (2009). For the power-law function, $y(t) = a(t - t_0)^{-b}$, we get $a = 138.0 \pm 2.1$ eV and $b = 0.04 \pm 0.01$. The result is shown in the lower left panel of Fig. 3. The lower right panel of Fig. 3 shows the fit of a broken power law. The best fit gives a normalization factor $a = 148.5 \pm 3.5$ eV with a break at 299 ± 73 d. The power-law index before and after the break point are 0.05 ± 0.01 and 0.03 ± 0.01, respectively. All the fitting parameters can be found in Table 3.

Degenaar et al. (2014) re-analysed the *Chandra* data of EXO 0748−676 used in Degenaar et al. (2011), also including the three *XMM–Newton* observations available at that time. They fitted these observations simultaneously, fixing the NS mass to $1.64\,M_\odot$ and the distance to the source to 7.1 kpc, which yielded a best-fitting NS radius of $13.2^{+0.6}_{-2.0}$ km. Because the NS mass and radius used in the fits by Degenaar et al. (2014) are different from those in Degenaar et al. (2011) that we used for Fig. 3, we cannot compare the temperatures in Degenaar et al. (2014) and those shown here (Fig. 3). We therefore re-fitted our spectra fixing the mass and radius to the values in Degenaar et al. (2014), and verified that the best-fitting parameters to the cooling curves that include the results of Degenaar et al. (2014) and ours are consistent with those in Table 3.

4 DISCUSSION

We analysed four *XMM–Newton* observations, from 2009 to 2013, of the NS LMXB EXO 0748−676 in quiescence. We fitted the X-ray spectra in the 0.3–10 keV range with the NS model atmosphere NSATMOS. If we fix the distance to 7.1 kpc (Galloway et al. 2008), the fit yields a χ^2 of 3774 for 3681 degrees of freedom, and the best-fitting mass and radius of the NS are $M_{\rm ns} = 2.00^{+0.07}_{-0.23}\,M_\odot$ and $R_{\rm ns} = 11.3 \pm 1.2$ km, respectively. Although this fit is statistically acceptable, we get a significantly better fit ($\chi^2 = 3620$ for 3675 degrees of freedom) with consistent values of the NS mass and radius, $M_{\rm ns} = 2.05^{+0.09}_{-0.39}\,M_\odot$ and $R_{\rm ns} = 11.4 \pm 2.1$ km, if we add a hot gas component to the model contributing 7–10 per cent of the total unabsorbed flux of the source in the 0.3–10.0 keV range. Combining the NS temperatures from our fits with those obtained by Degenaar et al. (2011) from *Chandra* and *Swift* observations, we find that the cooling curve of the NS in EXO 0748−676 is compatible with a model consisting either of an exponential decay plus a constant or a (broken) power law, although formally none of the models gives a good fit. We further found that no extra emission from a high-energy component, usually represented by a power law in the model, is required to fit the spectra of these four *XMM–Newton* observations, with a 95 per cent confidence upper limit of 1 per cent to the contribution of the power law to the total flux of the source in the 0.5–10.0 keV range.

We should mention that the choice of the table of solar abundance in the ISM and the distance to the source both significantly affect the best-fitting NS mass and radius. If we use the abundance table of Anders & Grevesse (1989) instead of the one of Wilms et al. (2000), the best-fitting mass and radius given by the NS hydrogen atmosphere model are $2.17^{+0.06}_{-0.13}\,M_\odot$ and $11.8^{+0.9}_{-1.2}$ km, respectively. The value of the distance we used in our analysis was obtained by Galloway et al. (2008b, see also Galloway et al. 2008a) from three PRE X-ray bursts of the source under the assumption of a canonical NS mass $M_{\rm ns} = 1.4\,M_\odot$ and radius $R_{\rm ns} = 10$ km. In fact, the determination of the distance not only depends upon the NS mass and radius, but also upon the hydrogen mass fraction of the burning fuel of the bursts. Assuming different hydrogen abundances in the burst fuel yields different values of the mass and radius. In addition, the angular distribution of the burst radiation, which was neglected by Galloway et al. (2008a), plays an important role in determining the source distance (Lapidus & Sunyaev 1985), and affects the best-fitting mass and radius significantly. The lowest energy of the spectra used in the analysis also has a strong impact on the best-fitting NS mass and radius in EXO 0748−676. We expand further on these issues in Section 4.3, and we will discuss this effect in more detail in a separate paper.

4.1 Residual emission near 0.5 keV

There is no significant edge in the effective area of the *XMM–Newton* instruments at this energy, which makes it unlikely that the residuals around 0.5 keV are instrumental. The residuals are still significant when we either use different cross-section and abundance tables or let the abundance of N, O, Ne and Fe in the interstellar medium free. The fits with the model CONST*PHABS*NSATMOS show significant residuals at ∼0.5 keV (see Fig. 1). To fit the residuals at around 0.5 keV, we included a hot gas component, VAPEC, in the model. The addition of this component improves the fits significantly; this component contributes ∼7–10 per cent of the total flux in the 0.3–10.0 keV range.

This hot collisionally ionized plasma could correspond to the absorption component reported by van Peet et al. (2009). They analysed the spectra of *XMM–Newton* observations during the outburst phase of this source and, by comparing the dipping and persistent spectra, they found that there are two absorbers in this system, one photoionized and one collisionally ionized. The latter should be located sufficiently far from the central source; for an assumed distance of $\sim 10^{11}$ cm away from the NS this gas would have a particle density $n > 10^{14}\,{\rm cm}^{-3}$, and does not change from persistent to

dipping states. From our fits with VAPEC, and assuming a geometry similar to that in van Peet et al. (2009), we find a particle density of $n \sim 10^{13}$ cm^{-3}. The temperature of this collisionally ionized plasma is around 150–270 eV, whereas van Peet et al. (2009) found a temperature between 60 and 80 eV. This difference could be due to the higher luminosity of the source in van Peet et al. (2009) compared to our observations, as the radiation from accretion during the outburst could cool down this plasma. This is also consistent with the findings of van Peet et al. (2009) that the column density increases significantly while this gas component is less ionized during the dips, as the material coming from the accretion stream cools down the plasma.

The residuals at ∼0.5 keV can also be fitted by adding a Gaussian component to the model as CONST*PHABS*(NSATMOS+GAUSSIAN). This model gives a moderately broad emission line with $E = 0.48 \pm 0.03$ keV and $\sigma = 0.09 \pm 0.03$ keV, with a χ^2 of 2627 for 3675 degrees of freedom ($N_{\rm H} = (7.9 \pm 0.9) \times 10^{20}$ cm^{-2}, $M_{\rm ns} = 2.14^{+0.07}_{-0.26}\,{\rm M}_{\odot}$, $R_{\rm ns} = 11.4 \pm 1.6$ km). The F-test probability for a chance improvement when adding a line to the model is 5×10^{-29}, which indicates that the addition of the Gaussian significantly improves the fit. As in the case of the VAPEC component, to check this we simulated 10^5 spectra of the model without the Gaussian line and fitted these spectra with the model that includes the line. None of these simulated spectra showed a line as strong (or stronger than) as the one we found from the fits to the data, which shows that the probability that the line is due to a statistical fluctuation is less than 10^{-5}.

The energy of the line, $E = 0.48 \pm 0.03$ keV, is consistent with the Lyα transition of N VII (rest energy of 0.500 keV). Maitra et al. (2011) reported a strong emission line near 0.5 keV in the spectrum of the transient LMXB MAXI J0556−332 in outburst. Maitra et al. (2011) concluded that the line in MAXI J0556−332 is due to N VII, and likely originates in material accreting from a donor star with an unusually high O/N abundance. Using the RGS spectrometer on board *XMM–Newton*, Cottam et al. (2001) found several emission lines, among them the N VII Lyα line, in the spectrum of EXO 0748−676 in outburst. Pearson et al. (2006) found a strong, 16.5Å equivalent width, NV λ1240 line in the *Hubble Space Telescope* spectrum, and Mikles & Hynes (2012) identified N III lines in the optical spectrum of EXO 0748−676 in outburst. All these results indicate significant nitrogen abundance in the companion star, UY Vol, supporting the identification of the line.

If the line is indeed from the source, and the N VII identification is correct, given the low luminosity of the source the highly ionized nitrogen must be produced by collisional ionization in a plasma at ∼0.1 keV or hotter (Cox & Tucker 1969). This high temperature rules out the surface of the companion star as the place where the line is formed, while the lack of a significant gravitational redshift rules out the NS atmosphere. On the other hand, the moderate width of the line in our fits suggests that the line may be produced in a residual accretion disc, or an advection-dominated accretion flows (ADAF; Narayan & Yi 1994; but see Menou & McClintock 2001) around the NS in quiescence. If this is indeed the case, the quiescent spectrum of EXO 0748−676 (and possibly other sources) may contain not only emission from the NS surface, but also from a weak accretion disc, which would significantly affect the study of cooling NSs in binary systems. Alternatively, if a residual disc is only present in EXO 0748−676, this could be the reason why the NS cooling process in this source appears to be less efficient than in the case of the NS in KS 1731–260, MXB 1659−29 and XTE J1701−462 (Degenaar et al. 2011; Díaz Trigo et al. 2011; Homan et al. 2014, see also Section 4.2).

4.2 The cooling of the neutron star in EXO 0748–676

After being heated by accretion during the outburst period in the quiescent phase, the crust of NSs in LMXBs takes several years to cool down and regain thermal equilibrium with the NS core (Yakovlev & Pethick 2004). In Fig. 3 we show the evolution of the NS temperature in EXO 0748−676 over a period of 5 yr in quiescence, after the source had been active for more than 20 yr. In this figure we included the data of the *XMM–Newton* observations analysed here, plus the temperatures obtained by Degenaar et al. (2011) using *Chandra* and *Swift*.

The cooling curve cannot be fitted with a simple exponential decay, whereas an exponential decay with a constant offset, a power law or a broken power-law decay all fit the data reasonably well. In the case of an exponential decay plus a constant, the e-folding time is 200 ± 27 d, and the constant temperature level is 106.2 ± 0.5 eV. The decay time provides the thermal relaxation time of the NS crust (Brown & Cumming 2009). Using *Chandra* and *Swift* data, Degenaar et al. (2014) found an e-folding time of 172 ± 52 d and a constant temperature level of 114.4 ± 1.2 eV while, based on the same first three observations presented here plus another *XMM–Newton* from 2008, Díaz Trigo et al. (2011) found an e-folding time of 133.5 ± 87.8 d and a constant base temperature of 109.1 ± 2.2 eV. Given that the NS temperature in the last observation of EXO 0748−676 presented here is already ∼105 eV, if it is the case, then the NS crust must already be close to the equilibrium temperature of the core. The three *Chandra* observations (Degenaar et al. 2014) between our last two *XMM–Newton* observations are consistent with this scenario. By fitting a blackbody model to a serendipitous Einstein IPC observation of EXO 0748−676 in quiescence taken in 1980, before it was discovered as a bright transient, Garcia & Callanan (1999) obtained a pre-outburst temperature of 220^{+140}_{-100} eV. Fitting an NSATMOS model simultaneously to the same pre-outburst Einstein and the post-outburst *Chandra* and *XMM–Newton* spectra, Degenaar et al. (2014) found a pre-outburst temperature of $94^{+5.6}_{-16.0}$ eV. If the latter is correct, a further decrease in temperature may be expected.

The cooling of EXO 0748−676 appears to be less pronounced than that of other sources (Degenaar et al. 2014; Homan et al. 2014). According to the numerical simulations of Brown & Cumming 2009, the NS cooling in these systems proceeds as a broken power law, with the initial power law being directly related to the thermal energy accumulated in the outer NS crust during outburst. Degenaar et al. (2011, see also Díaz Trigo et al. 2011) noted that the effective temperature of the other similar sources decreased by 20–40 per cent. Degenaar et al. (2014) discussed the possibility that the stalled cooling of EXO 0748−676 1 yr after the source entered quiescence may be due to either heat driven by convection in the outer layers of the NS (Medin & Cumming 2011, 2014), or the temperature profile in the crust not having reached a steady state at the end of the outburst. The latter mechanism would be applicable to sources that display short (∼1 yr) and very bright ($L \sim L_{\rm Edd}$) outbursts rather than to the case of EXO 0748−676, which was active for at least 24 yr accreting at less than ∼5 per cent the Eddington rate (Homan, Wijnands & van den Berg 2003). On the other hand, Schatz et al. (2014) identified a neutrino cooling mechanism in the NS crustal shell that is very sensitive to temperature. It may be possible that this mechanism plays a role in this case, since EXO 0748−676 is one of the two hottest crust cooling NS (Degenaar et al. 2014).

Our results suggest another possibility for the slow cooling of EXO 0748−676: if the emission line in the spectra of all our observations (see Section 4.1) is from the source, it suggests that

EXO 0748−676 may still be experiencing low-level accretion from a residual accretion disc in the quiescent phase. If this is correct, the emission in all observations of EXO 0748−676 in quiescence may actually be the combination of thermal emission from the NS and from a relatively cool accretion disc. From the width of the ∼0.5-keV Gaussian line, and assuming that the line is produced close to the inner edge of this putative disc, the inner radius of the disc would be ∼30–100 km for a NS mass in the range 1.4–2 $M_\odot$, and for disc temperatures of the order of 100 eV (Section 4.1), the disc would contribute ∼5–10 per cent of the 0.3–10 keV flux, and would therefore contaminate the thermal spectrum of the cooling NS. If this is the case, then this disc component may bring additional uncertainties in the NS mass and radius analysis.

Hynes & Jones (2009) detected a modulation in the quiescent optical and infrared light curves of EXO 0748−676 between 2008 November and 2009 January, with a period consistent with the X-ray orbital period of the source. They concluded that even in quiescence either the accretion disc or emission from the X-ray heated inner face of the companion star dominates the optical/infrared emission of this system. Bassa et al. (2009) found a broad component in the emission lines in a Doppler tomography study of EXO 0748−676 in the early phases of quiescence, which they interpreted as emission from a weak accretion disc. On the other hand, using observations later on in the quiescent state of EXO 0748−676, Ratti et al. (2012) did not detect the broad component reported by Bassa et al. (2009), and concluded that, at least at that time, there was no significant contribution from the accretion disc to the optical emission.

4.3 The power law

Degenaar et al. (2009) found that in a 2008 *Chandra* observation, just after EXO 0748−676 had turned into quiescence, besides the thermal component, a power-law component with an index of 1 contributed ∼16–17 per cent of the total 0.5–10 keV flux. A month after this *Chandra* observation, using an *XMM–Newton* observation Zhang et al. (2011, see also Díaz Trigo et al. 2011) found that a power-law component contributing ∼10 per cent of the total flux in the same energy band was required to fit the spectra. Furthermore, using *Chandra* data, Degenaar et al. (2011) found that the power-law component in their fits changed irregularly, decreasing significantly from 20 ± 3 per cent in 2008 October to 4 ± 3 per cent in 2009 June, and increasing again to 15 ± 4 per cent in 2010 April. A similar behaviour has also been observed in several NS X-ray binaries in quiescence, which has been interpreted as possible low-level accretion in these systems (Cackett et al. 2010a,b; Fridriksson et al. 2010).

EXO 0748−676 was observed five times in quiescence with *XMM–Newton*. The spectrum of the first observation, done almost immediately after accretion switched off, showed a thermal and a power-law component. Here we find that the spectra of the other four observations between 2009 and 2013 can be well described only by a thermal component (here we used the NS atmosphere model NSATMOS) and an emission line at ∼0.5 keV (see Section 3.1). Our fits do not require any power-law component, with a 95 per cent confidence upper limit of 1 per cent to the possible contribution of the power law to the 0.5–10.0 keV unabsorbed flux of the source. This upper limit is similar to those found by Díaz Trigo et al. (2011) in their fits of the first three observations presented here, and implies that, at least in EXO 0748−676, any possible accretion on to the magnetosphere or a shock from a pulsar wind (Campana et al. 1998) becomes negligible as the cooling process of the NS surface proceeds.

4.4 The mass and radius of the neutron star in EXO 0748–676

Degenaar et al. (2014) found an NS mass $M_{\rm ns} = 1.64 \pm 0.38\ M_\odot$ and a radius $R_{\rm ns} = 13.2^{+0.6}_{-2.0}$ km from fits to the quiescent spectra of EXO 0748−676 in the 0.5–10.0 keV band, whereas in our analysis we used the 0.3–10 keV band of the EPIC cameras; furthermore, Degenaar et al. (2014) did not include an additional component at around 0.5 keV in their model. Therefore, to study the influence of these factors upon the best-fitting mass, and to compare our results with those of Degenaar et al. (2014), we re-fitted our data both in the 0.3–10.0 keV and in the 0.5–10.0 keV band with the model CONST*PHABS*NSATMOS. In both cases we kept the distance to the source fixed at 7.1 kpc, similar to Degenaar et al. (2014). In the two panels of Fig. 4 we show the contour plots of the best-fitting NS mass and radius from this analysis. The left panel of this figure shows the result of the fits in the 0.3–10.0 keV band; the most likely mass and radius are $M_{\rm ns} = 2.08^{+0.07}_{-0.15}\ M_\odot$ and $R_{\rm ns} = 11.9 \pm 0.7$ km. As we mentioned in Section 3.1, these values are consistent with the ones for the model CONST*PHABS*(NSATMOS+VAPEC), which demonstrates that adding the hot gas component in the model does not have a significant effect in the best-fitting mass and radius of the NS. The right panel of Fig. 4 shows the result of the fits in the 0.5–10.0 keV band; in this case the most likely mass and radius are $M_{\rm ns} = 1.50^{+0.40}_{-0.99}\ M_\odot$ and $R_{\rm ns} = 12.2^{+1.0}_{-3.6}$ km, similar to the values found by Degenaar et al. (2014).

Our best-fitting mass is consistent with the value obtained by Özel (2006), $M_{\rm ns} = 2.10 \pm 0.28\ M_\odot$, based on the measurement of the Eddington luminosity at the peak of PRE bursts (Wolff et al. 2005) and redshifted absorption lines from the NS surface during bursts (Cottam, Paerels & Mendez 2002) (this spectral features could not be reproduced in a following observation; Cottam et al. 2008), and with the dynamical constraints of Muñoz-Darias et al. (2009), $1 \leq M_{\rm ns} \leq 2.40\ M_\odot$, and Bassa et al. (2009), $M_{\rm ns} \geq 1.27\ M_\odot$.

From fits to the EPIC plus RGS spectra of the first three observations presented here, plus the first *XMM–Newton* observation of EXO 0748−676 in quiescence (see Section 2), and for a distance of 7.1 kpc, Díaz Trigo et al. (2011) found $M_{\rm ns} = 1.77^{+0.4}_{-0.7}\ M_\odot$ and $R_{\rm ns} = 13.7 \pm 1.8$ km. On the other hand, from fits to EPIC data of the first *XMM–Newton* observation only, also for a distance of 7.1 kpc, Zhang et al. (2011) found $M_{\rm ns} = 1.55 \pm 0.12\ M_\odot$ and $R_{\rm ns} = 16.0^{+0.7}_{-1.3}$ km. We showed in Section 3 that the best-fitting NS mass does not change significantly whether we include the RGS data or not in the fits. The difference between our results and those of Díaz Trigo et al. (2011) and Zhang et al. (2011) must therefore come from the fact that the first *XMM–Newton* observation of EXO 0748−676 in quiescence requires a power-law component in the model, whereas no power-law component is needed to fit the four observations that we used here. A (mathematical) power law, as the one used in Díaz Trigo et al. (2011) and Zhang et al. (2011), extends all the way down to zero, whereas the true hard emission in this source, if present, should not extend below energies comparable to the NS temperature. It is then possible that the difference in the NS mass between this work and those of Díaz Trigo et al. (2011) and Zhang et al. (2011) is due to the fact that in those other papers part of the emission from the NS atmosphere was actually attributed to the power-law component.

Such a massive NS would in principle set very stringent constraints on the equation of state of nuclear matter (e.g. Lattimer & Prakash 2004). One should then review the assumptions that lead to this result to assess its reliability. The best-fitting mass and radius depend strongly on the assumed distance to the NS. Following Zhang et al. (2011) and Díaz Trigo et al. (2011), who used the

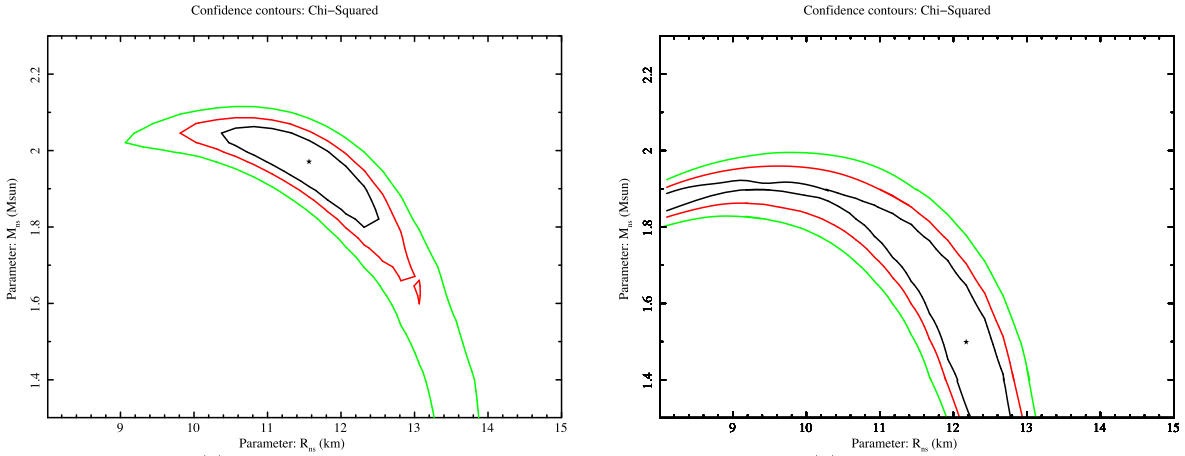

(a) 0.3-10.0 keV (b) 0.5-10.0 keV

Figure 4. Contour plots of the mass–radius relation of the NS in EXO 0748−676 based on the fits to the spectra in different energy ranges. We used the model CONST*PHABS*NSATMOS with the distance fixed to 7.1 kpc. The left panel is for the fit in the 0.3–10.0 keV energy range; the most likely mass and radius are $M_{\rm ns} = 1.99$ M$_\odot$ and $R_{\rm ns} = 11.3$ km, respectively. The right panel shows the result for the fit in the 0.5–10.0 keV energy band; the most likely mass and radius are $M_{\rm ns} = 1.50$ M$_\odot$ and $R_{\rm ns} = 12.2$ km, respectively. The three contour lines represent the confidence level of 68 per cent (black), 90 per cent (red) and 99 per cent (green) for two parameters.

distance from Galloway et al. (2008b), here we fixed the distance to 7.1 kpc; however, this number needs to be examined carefully.

The distance to EXO 0748−676 is based on the measured peak flux of a number of PRE bursts (Galloway et al. 2008b) under specific assumptions (see below) that may not be valid or may contradict the best-fitting mass and radius obtained assuming that distance. More specifically, to compute the Eddington luminosity (including the relativistic corrections) of the NSs in X-ray bursters, and to compare those luminosities with the peak flux of the PRE bursts in these sources, Galloway et al. (2008b) assumed a 1.4 M$_\odot$ and 10-km NS. These values are clearly inconsistent with the best-fitting values that we give here, and would indicate that the distance should be calculated iteratively. This is, unfortunately, not straightforward, because distances determined from PRE bursts also depend upon the hydrogen mass fraction, X, in the burst fuel, which is normally not known. Withal, the distances given in Galloway et al. (2008b), including the distance to EXO 0748−676, were computed under the assumption that the emission at peak of the bursts was isotropic (cf. Lapidus & Sunyaev 1985, Fujimoto 1988). EXO 0748−676 is a high-inclination system (see Section 1), and hence anisotropy will be very important in this case.

Galloway et al. (2008b) found that, for a 1.4 M$_\odot$ and 10-km NS, and for isotropic emission at the peak of the bursts, the distance to EXO 0748−676 can range between 7.4 ± 0.9 kpc for $X = 0$ and 5.7 ± 0.7 kpc for $X = 0.7$. If we, for instance, take the lowest value in that range, the best-fitting NS mass and radius in EXO 0748−676 are ∼1.6 M$_\odot$ and ∼6 km, respectively. Furthermore, measurements of the NS bolometric flux (and hence radius) through fits of the thermal emission of NSs with moderately high spin frequencies, like the NS in EXO 0748−676 that has a spin frequency of 552 Hz (Galloway et al. 2010), are affected by Doppler shift and frame dragging. Using equation (27) in Bauböck et al. (2015), our best-fitting NS radius would be about 2 per cent larger than inferred under the assumption that the star is not spinning. This, however, is the correction averaged over all possible inclination angles of the rotation axis of the NS with respect to the line of sight, whereas for high-inclination systems, as is likely the case of the NS in EXO 0748−676, the correction could be as large as 12 per cent (Bauböck et al. 2015). All the above shows that systematic errors in the deduced NS mass and radius are much larger than the statistical errors in our fits, and hence it would be disingenuous to take the best-fitting values that we obtain here at face value to draw strong conclusions about the nature of the interior of the NS in this system.

To investigate the effect of the minimum energy, $E_{\rm min}$, used in the spectral fits upon the deduced mass and radius, in Fig. 5 we show the best-fitting NS mass and radius of EXO 0748−676 using the model CONST*PHABS*NSATMOS for, respectively, $E_{\rm min}$ equal to 0.2, 0.3, 0.5 and 0.8 keV. This figure shows that the best-fitting NS mass decreases and the error in the mass increases as $E_{\rm min}$ increases. The best-fitting mass and error do not change significantly if $E_{\rm min}$ increases from 0.2 to 0.3 keV, but the error increases significantly if $E_{\rm min}$ increases from 0.3 to 0.5 keV. On the contrary, within errors, the best-fitting radius is independent of $E_{\rm min}$ when $E_{\rm min}$ varies between 0.2 and 0.8 keV, whereas the error in the best-fitting radius increases significantly as $E_{\rm min}$ increases from 0.2 to 0.5 keV. To understand this, in Fig. 6 we plot the flux density of the NSATMOS model versus energy for the four different values of the best-fitting mass shown in Fig. 5. We normalized the models such that the flux above 0.5 keV is the same in all four cases, which is equivalent to what one would get by fitting these four models to data above 0.5 keV. The vertical lines in this figure show the four values of $E_{\rm min}$ used in the fits to produce the plots in Fig. 5. From Fig. 6 it is apparent that the difference between the models increases as the energy decreases. Since the sensitivity to distinguish between two models with different values of the mass depends upon the area in between the curves of those two models, the sensitivity to the NS mass increases as $E_{\rm min}$ decreases, consistent with the fact that the errors in the NS mass decrease as $E_{\rm min}$ decreases (Fig. 5). Extending the fits down to the lowest possible energy is therefore crucial to accurately measure the NS mass using the NSATMOS model, and it is specially important in the case of EXO 0748−676 because the column density of the interstellar material towards the source is relatively low, therefore allowing us to observe the source down to very low energies. This must be balanced, however, with the lowest energy at which the instruments are accurately calibrated. Sartore et al. (2012) fitted the spectra of the isolated NS RX J1856.5−3754 using observations spanning a period of 10 yr, and they showed that the calibration of the EPIC cameras on board *XMM–Newton* is accurate down to

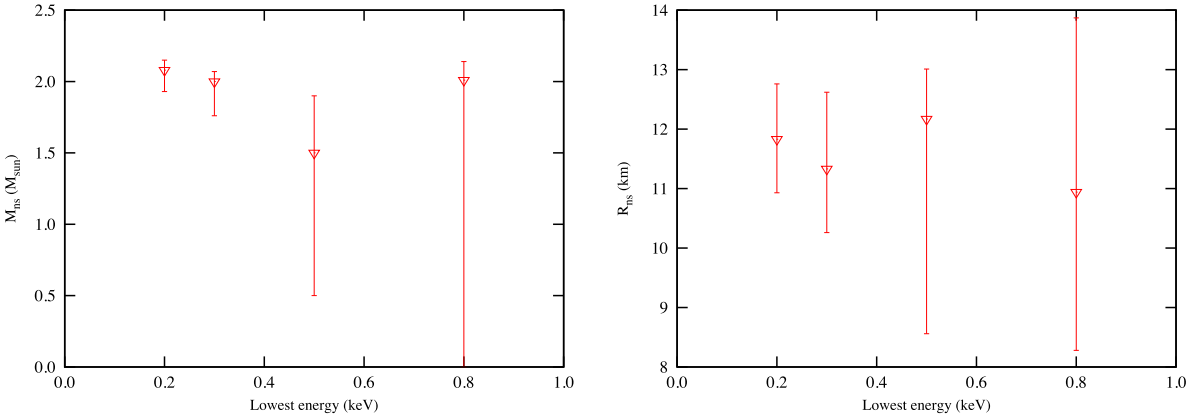

Figure 5. The best-fitting mass (left-hand panel) and radius (right-hand panel) of EXO 0748−676 obtained from fits with the model CONST*PHABS*NSATMOS (distance fixed to 7.1 kpc) when the minimum energy of the fits was, respectively, 0.2, 0.3, 0.5 and 0.8 keV. The best-fitting mass values are $2.08^{+0.07}_{-0.15}$, $2.00^{+0.07}_{-0.24}$, $1.50^{+0.40}_{-1.00}$ and $2.01^{+0.13}_{-2.01}$ $M_{\odot}$, respectively. The best-fitting values of radius are 11.8 ± 0.9, $11.3^{+1.3}_{-1.0}$, $12.2^{+0.8}_{-3.6}$ and $10.9^{+3.0}_{-2.6}$ km, respectively.

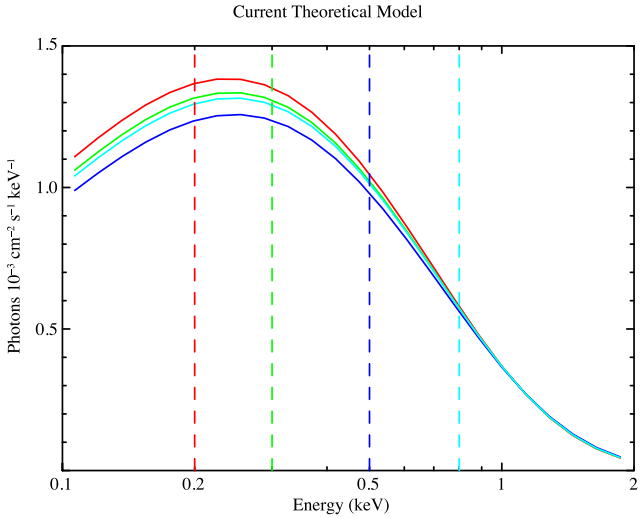

Figure 6. The NSATMOS model spectrum for the four values of the mass and radius obtained from the fits shown in Fig. 5. From top to bottom the models correspond to the fits with the lowest energy used in the fits equal to 0.2 keV (red), 0.3 keV (green), 0.8 keV (cyan) and 0.5 keV (blue). The models have been normalized so that the flux above 0.5 keV is the same for all of them.

5 per cent at 0.2 keV, and down to 3 per cent at 0.5 keV (see their fig. 1). A 5 per cent uncertainty in the calibration would add an extra uncertainty of ∼0.1 $M_{\odot}$ to the NS mass, which is much smaller than the statistical error obtained from the fits down to 0.5 keV, therefore justifying using data down to 0.2 keV.

ACKNOWLEDGEMENTS

This work is based on observations obtained with *XMM–Newton*, an ESA science mission with instruments and contributions directly funded by ESA Member States and the USA (NASA). This research made use of NASA's Astrophysics Data System. ZC acknowledges support by the Erasmus Mundus programme. MM wishes to thank MNM. We thank Laurence Boirin for commenting on the manuscript. We are very grateful to Matteo Guainazzi for helpful comments regarding the calibration of the EPIC instruments on board *XMM–Newton* and the correction for background flares. We thank the referee, Sebastien Guillot, for his careful reading of the manuscript and the very useful suggestions that helped us improve this paper.

This research has been funded with support from the European Commission. This publication reflects the views only of the author, and the Commission cannot be held responsible for any use which may be made of the information contained therein.

REFERENCES

Anders E., Grevesse N., 1989, Geochim. Cosmochim. Acta, 53, 197
Balucinska-Church M., McCammon D., 1992, ApJ, 400, 699
Bassa C. G., Jonker P. G., Steeghs D., Torres M. A. P., 2009, MNRAS, 399, 2055
Bauböck M., Özel F., Psaltis D., Morsink S. M., 2015, ApJ, 799, 22
Brown E. F., Cumming A., 2009, ApJ, 698, 1020
Cackett E. M., Brown E. F., Miller J. M., Wijnands R., 2010a, ApJ, 720, 1325
Cackett E. M., Brown E. F., Cumming A., Degenaar N., Miller J. M., Wijnands R., 2010b, ApJ, 722, L137
Campana S., Colpi M., Mereghetti S., Stella L., Tavani M., 1998, A&AR, 8, 279
Cottam J., Kahn S. M., Brinkman A. C., den Herder J. W., Erd C., 2001, A&A, 365, L277
Cottam J., Paerels F., Mendez M., 2002, Nature, 420, 51
Cottam J., Paerels F., Méndez M., Boirin L., Lewin W. H. G., Kuulkers E., Miller J. M., 2008, ApJ, 672, 504
Cox D. P., Tucker W. H., 1969, ApJ, 157, 1157
Degenaar N. et al., 2009, MNRAS, 396, L26
Degenaar N. et al., 2011, MNRAS, 412, 1409
Degenaar N. et al., 2014, ApJ, 791, 47
den Herder J. W. et al., 2001, A&A, 365, L7
Díaz Trigo M., Boirin L., Costantini E., Méndez M., Parmar A., 2011, A&A, 528, A150
Fridriksson J. K. et al., 2010, ApJ, 714, 270
Fujimoto M. Y., 1988, ApJ, 324, 995
Galloway D. K., Özel F., Psaltis D., 2008a, MNRAS, 387, 268
Galloway D. K., Muno M. P., Hartman J. M., Psaltis D., Chakrabarty D., 2008b, ApJS, 179, 360
Galloway D. K., Lin J., Chakrabarty D., Hartman J. M., 2010, ApJ, 711, L148
Garcia M. R., Callanan P. J., 1999, AJ, 118, 1390
Gottwald M., Haberl F., Parmar A. N., White N. E., 1986, ApJ, 308, 213
Haensel P., Zdunik J. L., 2008, A&A, 480, 459
Heinke C. O., Rybicki G. B., Narayan R., Grindlay J. E., 2006, ApJ, 644, 1090
Homan J., van der Klis M., 2000, ApJ, 539, 847

Homan J., Wijnands R., van den Berg M., 2003, A&A, 412, 799
Homan J., Fridriksson J. K., Wijnands R., Cackett E. M., Degenaar N., Linares M., Lin D., Remillard R. A., 2014, ApJ, 795, 131
Hynes R. I., Jones E. D., 2009, ApJ, 697, L14
Lapidus I. I., Sunyaev R. A., 1985, MNRAS, 217, 291
Lattimer J. M., Prakash M., 2004, Science, 304, 536
Maitra D., Miller J. M., Raymond J. C., Reynolds M. T., 2011, ApJ, 743, L11
Medin Z., Cumming A., 2011, ApJ, 730, 97
Medin Z., Cumming A., 2014, ApJ, 783, L3
Menou K., McClintock J. E., 2001, ApJ, 557, 304
Mikles V. J., Hynes R. I., 2012, ApJ, 750, 132
Muñoz-Darias T., Casares J., O'Brien K., Steeghs D., Martínez-Pais I. G., Cornelisse R., Charles P. A., 2009, MNRAS, 394, L136
Narayan R., Yi I., 1994, ApJ, 428, L13
Özel F., 2006, Nature, 441, 1115
Parmar A. N., White N. E., Giommi P., Gottwald M., 1986, ApJ, 308, 199
Pearson K. J. et al., 2006, ApJ, 648, 1169
Piconcelli E., Jimenez-Bailón E., Guainazzi M., Schartel N., Rodríguez-Pascual P. M., Santos-Lleó M., 2004, MNRAS, 351, 161
Protassov R., van Dyk D. A., Connors A., Kashyap V. L., Siemiginowska A., 2002, ApJ, 571, 545
Ratti E. M., Steeghs D. T. H., Jonker P. G., Torres M. A. P., Bassa C. G., Verbunt F., 2012, MNRAS, 420, 75
Sartore N., Tiengo A., Mereghetti S., De Luca A., Turolla R., Haberl F., 2012, A&A, 541, A66
Schatz H. et al., 2014, Nature, 505, 62
Sidoli L., Parmar A. N., Oosterbroek T., 2005, A&A, 429, 291
Smith R. K., Brickhouse N. S., Liedahl D. A., Raymond J. C., 2001, ApJ, 556, L91
Strüder L. et al., 2001, A&A, 365, L18
van Peet J. C. A., Costantini E., Méndez M., Paerels F. B. S., Cottam J., 2009, A&A, 497, 805
Verner D. A., Ferland G. J., Korista K. T., Yakovlev D. G., 1996, ApJ, 465, 487
Villarreal A. R., Strohmayer T. E., 2004, ApJ, 614, L121
Wilms J., Allen A., McCray R., 2000, ApJ, 542, 914
Wolff M. T., Becker P. A., Ray P. S., Wood K. S., 2005, ApJ, 632, 1099
Wolff M. T., Ray P. S., Wood K. S., 2008a, Astron. Telegram, 1736, 1
Wolff M., Ray P., Wood K., Wijnands R., 2008b, Astron. Telegram, 1812, 1
Yakovlev D. G., Pethick C. J., 2004, ARA&A, 42, 169
Yan M., Sadeghpour H. R., Dalgarno A., 1998, ApJ, 496, 1044
Zhang G., Méndez M., Jonker P., Hiemstra B., 2011, MNRAS, 414, 1077

This paper has been typeset from a TEX/LATEX file prepared by the author.